Electronic Structure Engineering of Honeycomb Layered Cathode Material for Sodium-Ion Batteries

Natalia Voronina,[a] Hee Jae Kim,[b] Najma Yaqoob,[b] Olivier Guillon,[b] Payam Kaghazchi[b,*], Seung-Taek Myung[a,*]

[a]*Hybrid Materials Research Center, Department of Nanotechnology and Advanced Materials Engineering & Sejong Battery Institute, Sejong University, 98 Gunja-dong, Gwangjin-gu, Seoul 05006, South Korea*
[b]*Forschungszentrum Jülich GmbH, Institute of Energy and Climate Research, Materials Synthesis and Processing (IEK-1), Jülich, Germany*

*Corresponding author
E-mail: p.kaghazchi@fz-juelich.de (P. Kaghazchi), smyung@sejong.ac.kr (S. Myung)

Abstract

In this work, we introduce a rational design of O'3-type $Na[Ni_{2/3-x}Co_xSb_{1/3}]O_2$, which is a solid solution of $Na[Ni_{2/3}Sb_{1/3}]O_2$ – $Na[Co_{2/3}Sb_{1/3}]O_2$. Adopting the difficulty of $Co^{3+/2+}$ redox reaction, the electronic structure of $Na[Ni_{2/3-x}Co_xSb_{1/3}]O_2$ compounds are engineered to build electro-conducting networks in the oxide matrix through electrochemical oxidation of Co^{2+} to Co^{3+}, after which the formed Co^{3+} does not participate in the electrochemical reaction but improve electric conductivity in the structure. Density functional theory calculation reveals reduced band gap energy after formation of Co^{3+} on desodiation of the $Na_{1-y}[Ni_{2/3-x}Co_xSb_{1/3}]O_2$. Expensing the $Co^{3+/2+}$ redox while improving electric conductivity, the $Na[Ni_{2/3-x}Co_xSb_{1/3}]O_2$ (x = 1/6) electrode boosts excellent cyclability for 1,000 cycles with ~72.5 % retention at 2 C (400 mA g^{-1}) and activity even at 50 C (10 A g^{-1}) in Na cells. *Operando* X-ray diffraction and *ex-situ* X-ray absorption near edge structure investigations reveal reduced lattice variations upon charge and discharge by the presence of electrochemical-driven Co^{3+} in the structure, compared with the $Na[Ni_{2/3}Sb_{1/3}]O_2$. These findings offer a new strategy for the development of cathode materials, providing important insights on structural transformations and electronic nature in advanced cathode materials.

Keywords: Layer; Cathode; Electronic Structure; Sodium; Battery.

1. Introduction

Natural abundance of sodium resources has arose significant attention for the development of high performance cathode materials such as layered metal oxides,[1-3] polyanionic compounds,[4-7] and Prussian blue analogues[8,9] for sodium-ion batteries (SIBs). Many of polyanion compounds have utilized their intrinsic inductive effect, which raises the operation voltages in Na cells.[10,11] Despite their small capacity, achievement of high energy density for cycling results from the structural stability by the presence of covalent polyanions in the structure.[12,13] Prussian blue analogues also demonstrate acceptable cycling stability for long term. However, elaboration is required to improve the low tap density of those materials to the levels of layered transition metal oxides or polyanion compounds in consideration of energy density for SIBs.[14] Layered compounds typically crystallize into P2 and O3 structures, in which Mn in transition metal layer is significant to provide initial high capacity or structural stability depending on the oxidation state in compounds.[15,16] Meanwhile, those Mn-based layer compounds suffer from inevitable adsorption of water molecules in air and structural instability ascribed to Jahn-Teller distortion of Mn^{3+} that elongates the Mn-O distance in MnO_6 along the *z*-axis.[17] In addition, multi-step phase transitions are not desirable because the accompanied large volume changes affect breakdown of the crystal structure to not be available for long term cycles.[18-20] In particular, for P2 and P3 layer compounds, the deficient sodium content in the compound is a critical drawback to cause a small charge capacity at the first charge, and this simultaneously arises abnormal first Coulombic efficiency. Additives can compensate for the deficient sodium for the insufficient charge capacity, while decomposition of those additives is incline to leave pores in cathodes that increase internal resistance after the first charge. [21-22] Therefore, the capacity belonging to the deficient sodium cannot be utilized in full cells, without additional treatments such as pre-sodiation of cathodes.

This recalls layered O3-type compounds, the octahedrally coordinated sodium with its

sufficient amount between the transition metal slabs in the structure. One of the O3-type analogues is O'3 $NaNiO_2$, which crystallizes into monoclinic symmetry due to the Jahn-Teller distortion of the Ni^{3+}, which is less influential than Mn^{3+}, and possesses relatively high theoretical capacity and operating voltage.[23,24] On the contrary, the O'3 $NaNiO_2$ undergoes multiple O'3-P'3-P"3-O"3-O"'3 phase transitions during desodiation, while experiencing gradual capacity fade during cycling. [23] To mitigate these issues, earlier works have investigated to introduce different electro-active (Co,[25-28] Mn,[28-30] Fe,[25,31] and Cu[32]) and electro-inactive (Mg,[31,33] Zn,[32,34] Al,[26,27] Bi,[35,36] Sn,[29,37] and Sb[33,38] elements. One of the interesting examples that improves structural, air sensitivity, and thermal stability of $NaNiO_2$ is the introduction of a third of Sb^{5+} into the Ni^{2+} sites to form the O'3-$Na[Ni_{2/3}Sb_{1/3}]O_2$ layered material.[39] The low oxidation state of Ni^{2+} (0.69 Å) and high oxidation state of Sb^{5+} (0.6 Å), with the difference in ionic radius and the ratio Ni^{2+}:Sb^{5+} = 2:1, promote the formation of honeycomb-ordered superstructure in the Ni_2SbO_6 layer. The intense electrostatic repulsion between Ni^{2+} and Sb^{5+} is beneficial for increasing the operation voltage, compared to $NaNiO_2$; namely, two discharge plateaus at 3.3 and 3.7 V attributed to the reversible insertion of 0.67 Na^+ accompanied by a $Ni^{2+/3+}$ redox pair (theoretically 132 mAh g^{-1}) through the O'3-P'3-O1 phase transition.[38] Improved structural stability of $Na[Ni_{2/3}Sb_{1/3}]O_2$ cathode have been achieved by substituting Ni^{2+} with inactive elements such as Zn^{2+} and Mg^{2+}, suppressing the P'3-O1 phase transition corresponding to the voltage plateau emerged at 3.7 V.[33,34]

We rationally optimize the O'3-$Na[Ni_{2/3}Sb_{1/3}]O_2$ through substitution of Ni^{2+} by Co^{2+}. The similar ionic radii and valence of Ni^{2+} (0.69 Å) and Co^{2+} (0.74 Å) render homogeneous incorporation of Co^{2+} into the metal layers in O'3-$Na[Ni_{2/3-x}Co_xSb_{1/3}]O_2$ (x = 0 – 2/3). Similar to $Na[Ni_{2/3}Sb_{1/3}]O_2$, the delivered charge capacity was about 132 mAh (g-oxide)$^{-1}$ at 10 mA g^{-1} (0.05C) for the Co-substituted $Na[Ni_{2/3-x}Co_xSb_{1/3}]O_2$ (x = 1/6) ascribed to the oxidation of Ni^{2+} to Ni^{3+} and Co^{2+} to Co^{3+} on charge. The oxidation of Co raises the average operation

voltage from 3.6 V to 3.9V for the upper voltage plateau. The formed Co^{3+} does not participate in the electrochemical capacity during discharge, whaereas the reduction of Ni^{3+} to Ni^{2+} was the only electro-active species for discharging to 2 V. Simultaneously, the electrochemical-driven Co^{3+} provides electro-conductive networks in the oxide matrix, enabling that $Na[Ni_{2/3-x}Co_xSb_{1/3}]O_2$ (x = 1/6) presents acceptable electrochemical performance, namely, ~ 93 % capacity retention at 0.05C for 100 cycles and ~72.5% for 1000 cycles at 2C (400 mA g^{-1}) achieved by the Ni^{3+}/Ni^{2+} redox pair, as confirmed by X-ray absorption near edge structure spectroscopy (XANES). *Operando* X-ray diffraction (*O*-XRD), transmission electron microscopy (TEM), and first principle calculations show that electrochemically generated Co^{3+}, which was maintained during subsequent cycles, endorses not only the electrical conductivity of $Na_{1-y}[Ni_{1/2}Co_{1/6}Sb_{1/3}]O_2$ but also less unit volume change in the crystal structure than the $Na[Ni_{2/3}Sb_{1/3}]O_2$ during charge and discharge. We herein investigate the efficacy of electrochemical-driven Co^{3+} that affects structure and electrochemical performance of $Na[Ni_{2/3-x}Co_xSb_{1/3}]O_2$ as a cathode material for SIBs.

2. Results and Discussion

Powder X-ray diffraction (XRD) data of as-synthesized $Na[Ni_{2/3-x}Co_xSb_{1/3}]O_2$ (x = 0 – 2/3) were analyzed by Rietveld refinement program, Fullprof, assuming monoclinic structure with *C2/m* space group (**Figure 1a**). For the refinement, Ni, Co, and Sb ions occupied the octahedral sites, and the refinement results showed that the observed pattern coincided with the calculated one. The observed peaks between 2θ = 20 –30° related to the superstructure, which appear for all compounds in this series, indicates cationic ordering Sb/Ni(Co) in the structure. The calculated lattice parameters (*a*, *b*, and *c*) linearly increased with increasing the Co content (**Figure 1b**), obeying Vegard's law as a result of solid solution formation between

$Na[Ni_{2/3}Sb_{1/3}]O_2$ and $Na[Co_{2/3}Sb_{1/3}]O_6$. In consideration of ionic radii of Ni^{2+} (0.69 Å) and Co^{2+} (low spin: 0.65 Å and high spin: 0.745 Å), it is reasonable that the larger Co^{2+} (high spin: 0.745 Å) substitutes the Ni^{2+} in the metal layer of $Na[Ni_{2/3-x}Co_xSb_{1/3}]O_2$ (x = 0 – 2/3). Details of structural parameters are described in **Table S1 and S2**. The average oxidation states of Ni and Co indicate that Ni and Co are stabilized as Ni^{2+} and Co^{2+} in $Na[Ni_{2/3-x}Co_xSb_{1/3}]O_2$ (x = 1/6) compounds (**Figure 1c and 1d**). Scanning electron microscopy (SEM) and transmission electron microscopy (TEM) analyses revealed homogeneous distribution of Na, Ni, Co, Sb and O elements in $Na[Ni_{1/2}Co_{1/6}Sb_{1/3}]O_2$ (**Figure 1f and S1**).

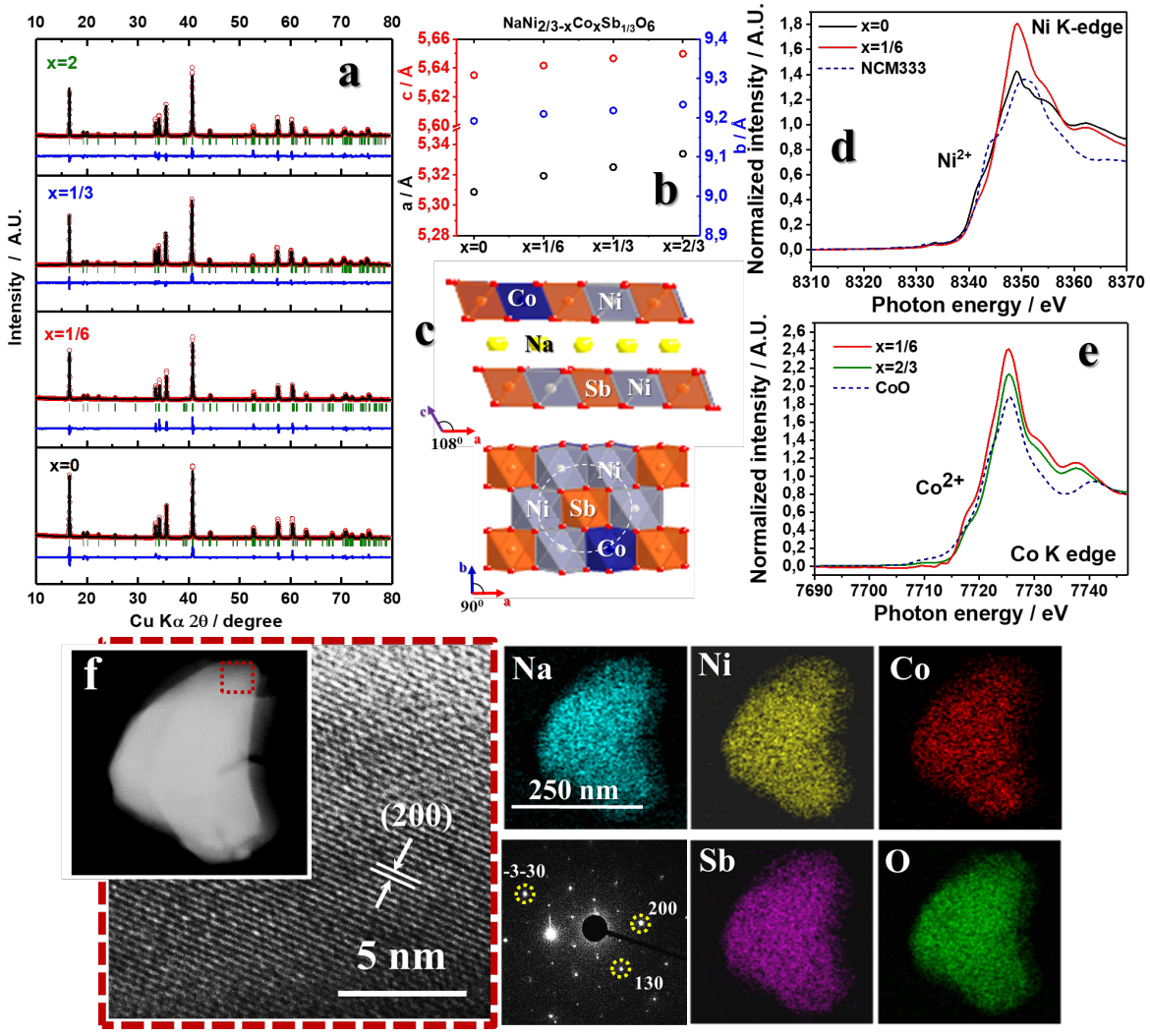

Figure 1. (a) Rietveld refinement results of XRD data for $Na[Ni_{2/3-x}Co_xSb_{1/3}]O_2$ and (b) the

corresponding calculated lattice parameters; XANES spectra of (c) Ni K-edge and (d) Co K-edge spectra for $Na[Ni_{2/3-x}Co_xSb_{1/3}]O_6$ (x = 0, 1/6, and 2/3); (e) crystal structure of $Na[Ni_{1/2}Co_{1/6}Sb_{1/3}]O_2$ drawn using the data obtained from Rietveld refinement of XRD data and DFT calculation; (f) TEM images of $Na[Ni_{2/3-x}Co_xSb_{1/3}]O_2$ (x = 1/6) with HR-TEM image selected-area electron diffraction pattern taken along [001] zone axis and EDS mappings of Na, Ni, Co, Sb, and O.

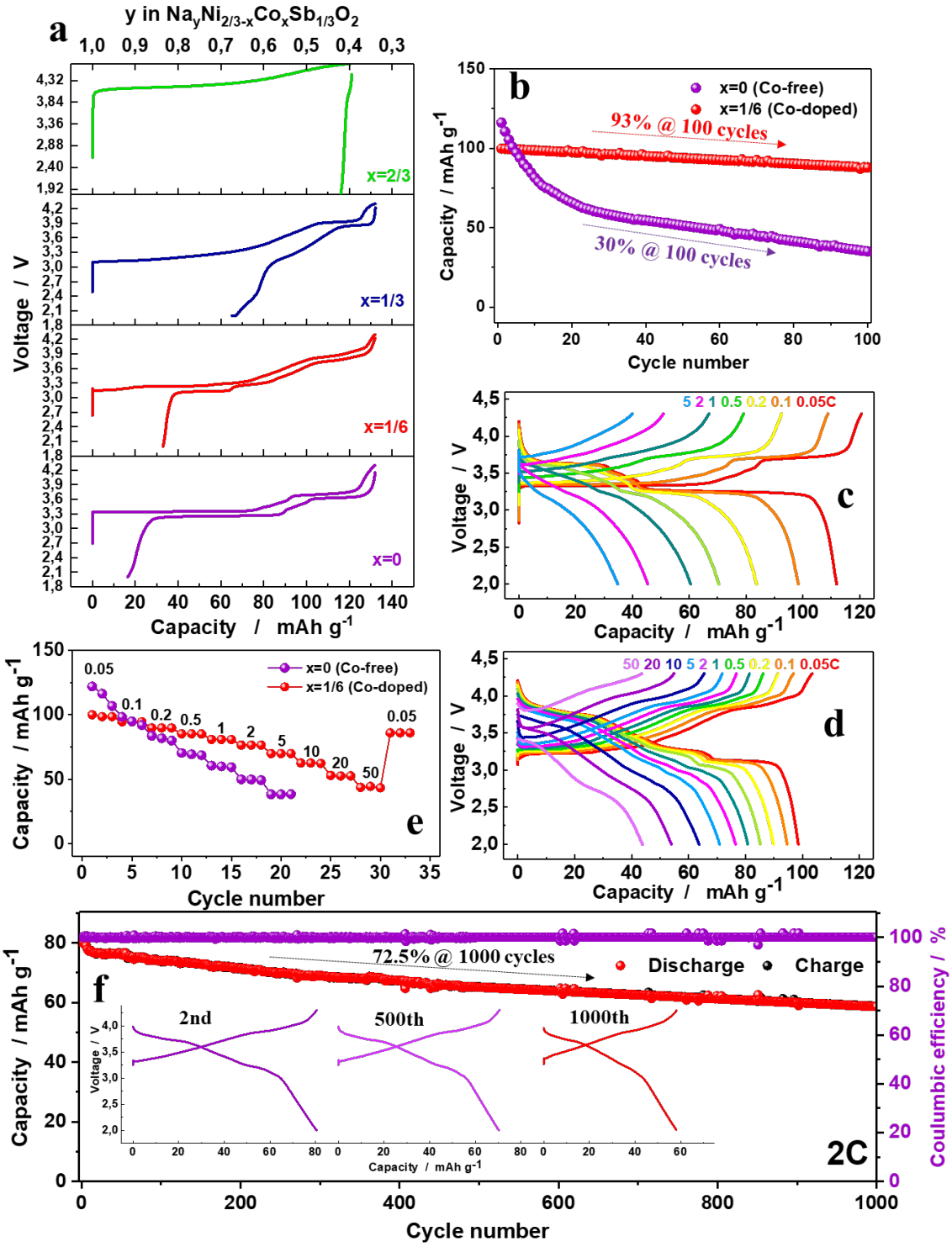

Figure 2. (a) First charge and discharge curves of $Na[Ni_{2/3-x}Co_xSb_{1/3}]O_2$ (x = 0, 1/6, and 1/2) tested in the voltage range of 2–4.3 V and $Na[Ni_{2/3-x}Co_xSb_{1/3}]O_2$ (x = 2/3) operated between 2 – 4.6 V at a current of 10 mA g^{-1} and (b) the corresponding cycling stability of $Na[Ni_{2/3-x}Co_xSb_{1/3}]O_2$ (x = 0 and 1/6) measured at 0.05 C (10 mA g^{-1}); (c) rate capability of $Na[Ni_{2/3}Sb_{1/3}]O_2$, (d) $Na[Ni_{2/3-x}Co_xSb_{1/3}]O_2$ (x = 1/6), and (e) the resulting cycling data of $Na[Ni_{2/3-x}Co_xSb_{1/3}]O_2$ (x = 0 and 1/6) from 0.05 to 50 C-rates; (f) long term cycling performance of $Na[Ni_{1/2}Co_{1/6}Sb_{1/3}]O_2$ at 2 C-rates.

The electrochemical performances of $Na[Ni_{2/3-x}Co_xSb_{1/3}]O_2$ (x = 0 – 2/3) were investigated between 2 – 4.3 V at 10 mA g^{-1} (0.05 C) (**Figure 2a**). For the Co-free $Na[Ni_{2/3}Sb_{1/3}]O_2$, the charge–discharge voltage profile shows a reversible two-step variation. The delivered charge capacity was 132 mAh g^{-1}, which is solely ascribed to the oxidation of Ni^{2+} to Ni^{3+} and on discharge *vice versa*.[38] The charge capacity of the $Na[Ni_{2/3}Sb_{1/3}]O_2$ was identical to those of x = 1/6 and 1/3 in $Na[Ni_{2/3-x}Co_xSb_{1/3}]O_2$, whereas the $Na[Ni_{2/3-x}Co_xSb_{1/3}]O_2$ (x = 2/3) exhibited 120 mAh g^{-1} with a single voltage plateau which resulted from the oxidation of Co^{2+} to Co^{3+}. This implies that the oxidation of Co^{2+} to Co^{3+} increases the capacity during charge. On the contrary, discharge capacity decreased with increasing the Co content in $Na[Ni_{2/3-x}Co_xSb_{1/3}]O_2$ (x = 1/6, 1/3, and 2/3), and the capacity was negligible for the $Na[Co_{2/3}Sb_{1/3}]O_2$. The observed decrease in capacity with increasing Co content may result from difficulty of the reduction Co^{3+} to Co^{2+} on discharge in the voltage range of 2 – 4.3 V. Apart from the discharge capacity, two voltage plateaus were evident on discharge except for the Ni-free $Na[Co_{2/3}Sb_{1/3}]O_2$. Another interesting feature is that the upper voltage plateau increased from 3.6 V for $Na[Ni_{2/3}Sb_{1/3}]O_2$ to 3.9 V for $Na[Ni_{2/3-x}Co_xSb_{1/3}]O_2$ (x = 1/6 and 1/3).

Although the Co-free $Na[Ni_{2/3}Sb_{1/3}]O_2$ (x=0, 116 mAh g^{-1}) delivered a higher discharge capacity than that of the $Na[Ni_{2/3-x}Co_xSb_{1/3}]O_2$ (x = 1/6, 99 mAh g^{-1}), the capacity rapidly degraded during cycles for the Co-free $Na[Ni_{2/3}Sb_{1/3}]O_2$, retaining as low as 30 % of the first capacity after 100 cycles (**Figure 2b**); however, the Co-substituted $Na[Ni_{2/3-x}Co_xSb_{1/3}]O_2$ (x = 1/6) demonstrated significant improvement in capacity retention for 100 cycles, 93 % of the

first capacity). The rate capability was evaluated at 0.05C – 50 C (10 – 10,000 mA g^{-1}) in **Figure 2 c-e**. Unfortunately, the Co-free $Na[Ni_{2/3}Sb_{1/3}]O_2$ was inactive over a 5 C-rate (1 A g^{-1}). On the contrary, the Co-substituted $Na[Ni_{1/2}Co_{1/6}Sb_{1/3}]O_2$ electrode was able to show its activity up to 50 C-rates (10 A g^{-1}), delivering about 45 mAh g^{-1}. It is notable that the Co-substituted $Na[Ni_{1/2}Co_{1/6}Sb_{1/3}]O_2$ demonstrates the extraordinary cycling stability at a 2 C-rate (400 mA g^{-1}) that retains ~72.5 % of the initial capacity over 1,000 cycles (**Figure 2f**). Overall, the present Co-substitution in $Na[Ni_{2/3}Sb_{1/3}]O_2$ significantly improves cycling stability and rate capability.

Operando XRD analysis was carried out to understand the structural change for $Na[Ni_{2/3-x}Co_xSb_{1/3}]O_2$ (x = 0 and 1/6) during de-/sodiation (**Figure 3**). For the Co-free $Na[Ni_{2/3}Sb_{1/3}]O_2$ electrode (**Figure 3a**), as sodium ions were extracted from the structure to y = 0.19 in $Na_{1-y}[Ni_{2/3}Sb_{1/3}]O_2$, there was emergence of a new P'3 phase. These two phases, O'3 and P'3, prevail along the plateau on 3.3 V to y = 0.36 in $Na_{1-y}[Ni_{2/3}Sb_{1/3}]O_2$, after which the O'3 was no more visible but the P'3 phase became the dominant phase to y = 0.57 in $Na_{1-y}[Ni_{2/3}Sb_{1/3}]O_2$ on the upper voltage plateau, ~3.6 V. Further desodiation resulted in formation of a new phase, O1, maintained to y = 0.34 in $Na_{1-y}[Ni_{2/3}Sb_{1/3}]O_2$. The phase transition was reversible on discharge; namely, O1 – P'3 – O'3, reaching O'3-$Na_{0.92}[Ni_{2/3}Sb_{1/3}]O_2$.

For $Na[Ni_{1/2}Co_{1/6}Sb_{1/3}]O_2$, the phase transition occurred more complicated on charge (**Figure 4b**). The O'3 phase was transformed to hexagonal O3 phase from y = 0.07 in $Na_{1-y}[Ni_{1/2}Co_{1/6}Sb_{1/3}]O_2$ of which the O3 phase was refined at y = 0.1 in $Na_{1-y}[Ni_{1/2}Co_{1/6}Sb_{1/3}]O_2$ (**Figure 4c-1**). The O'3 and the new O3 phases coexisted to y = 0.19 in $Na_{1-y}[Ni_{1/2}Co_{1/6}Sb_{1/3}]O_2$ that showed the growth of the Bragg peaks at 16.3°, 32.9°, 34.8°, 36.1°, and 41.1° (2θ) of (003), (006), $(01\bar{1})$ and $(01\bar{4})$ planes for the O3 phase, respectively, together with the Bragg peaks at 16.5°, 33.4°, 34.3°, 35.7°, and 40.8° (2θ) of (001), (002), (130), (131) and $(13\bar{1})$ planes,

respectively, of the initial O'3 phase. Further desodiation induced the formation of P'3 phase, which presented together with the O'3 and O3 phase to y = 0.28 in $Na_{1-y}[Ni_{1/2}Co_{1/6}Sb_{1/3}]O_2$. The disappearance of O'3-O3 phases further led to the solid solution behavior of P'3 with a linear shift of the (001) and (002) reflections to the lower angles while the $(13\bar{1})$ ad (130) reflections toward the higher angles. Note that the regime of P'3 phase, refined in **Figure 4c-2**, was extended from y = 0.19 – 0.62 in $Na_{1-y}[Ni_{1/2}Co_{1/6}Sb_{1/3}]O_2$, compared to the region of P'3 phase from y = 0.19 – 0.57 in $Na_{1-y}[Ni_{2/3}Sb_{1/3}]O_2$. Meanwhile, the O1 phase, refined in **Figure 4c-3**, was dominant in the short range, y = 0.62 – 0.66 in $Na_{1-y}[Ni_{1/2}Co_{1/6}Sb_{1/3}]O_2$ on charge, which is highlighted in **Figure S2**. Therefore, the $Na[Ni_{1/2}Co_{1/6}Sb_{1/3}]O_2$ delivered the charge capacity 132 mAh g^{-1} *via* the multiple phase transition of O'3 – O3 –P'3 – O1. Upon discharge, the charged $Na_{0.34}[Ni_{1/2}Co_{1/6}Sb_{1/3}]O_2$ was return to hexagonal O3 phase $Na_{0.84}[Ni_{1/2}Co_{1/6}Sb_{1/3}]O_2$ (**Figure 4b**); however, there was emergence of the original O'3 phase. The refinement of the phase agreed well with the hexagonal $R\bar{3}m$ symmetry with lattice parameters a = 3.0161(2) Å and c = 16.2259(7) Å. This summarizes that the sodiation resulted in the continuous phase transition of O1 – P'3 – O3, which did not recover to the initial O'3 phase.

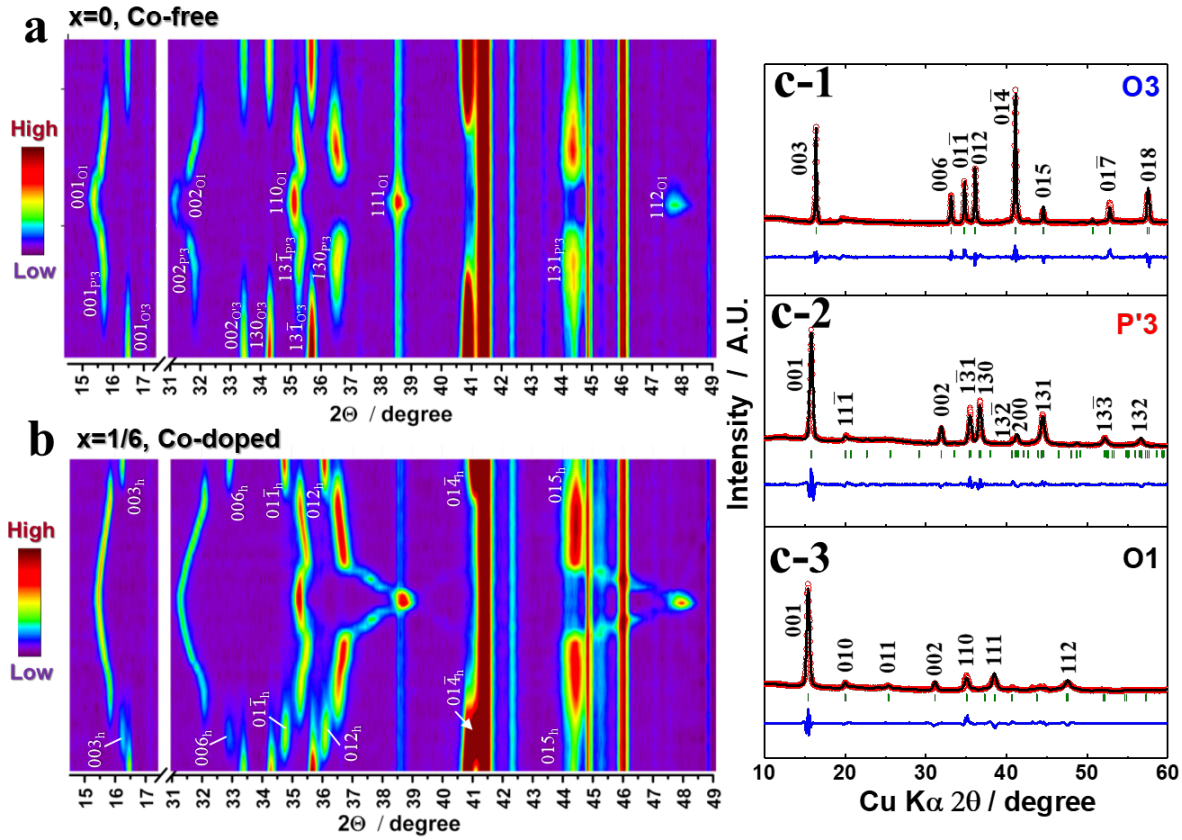

Figure 3. Structural evolution of $NaNi_{2/3-x}Co_xSb_{1/3}O_2$: 2D image of *operando* XRD data during the first cycle for (a) $x = 0$ and (b) $x = 1/6$ in $Na[Ni_{2/3-x}Co_xSb_{1/3}]O_2$ (*- break from peaks of Al current collector and Be-window); Rietveld refinement results of XRD data for $Na[Ni_{1/2}Co_{1/6}Sb_{1/3}]O_2$; (c-1) hexagonal O3 charge to 3.3 V; (c-2) monoclinic P'3 charged to 3.7 V; (c-3) hexagonal O1 phase charge to 4.3 V.

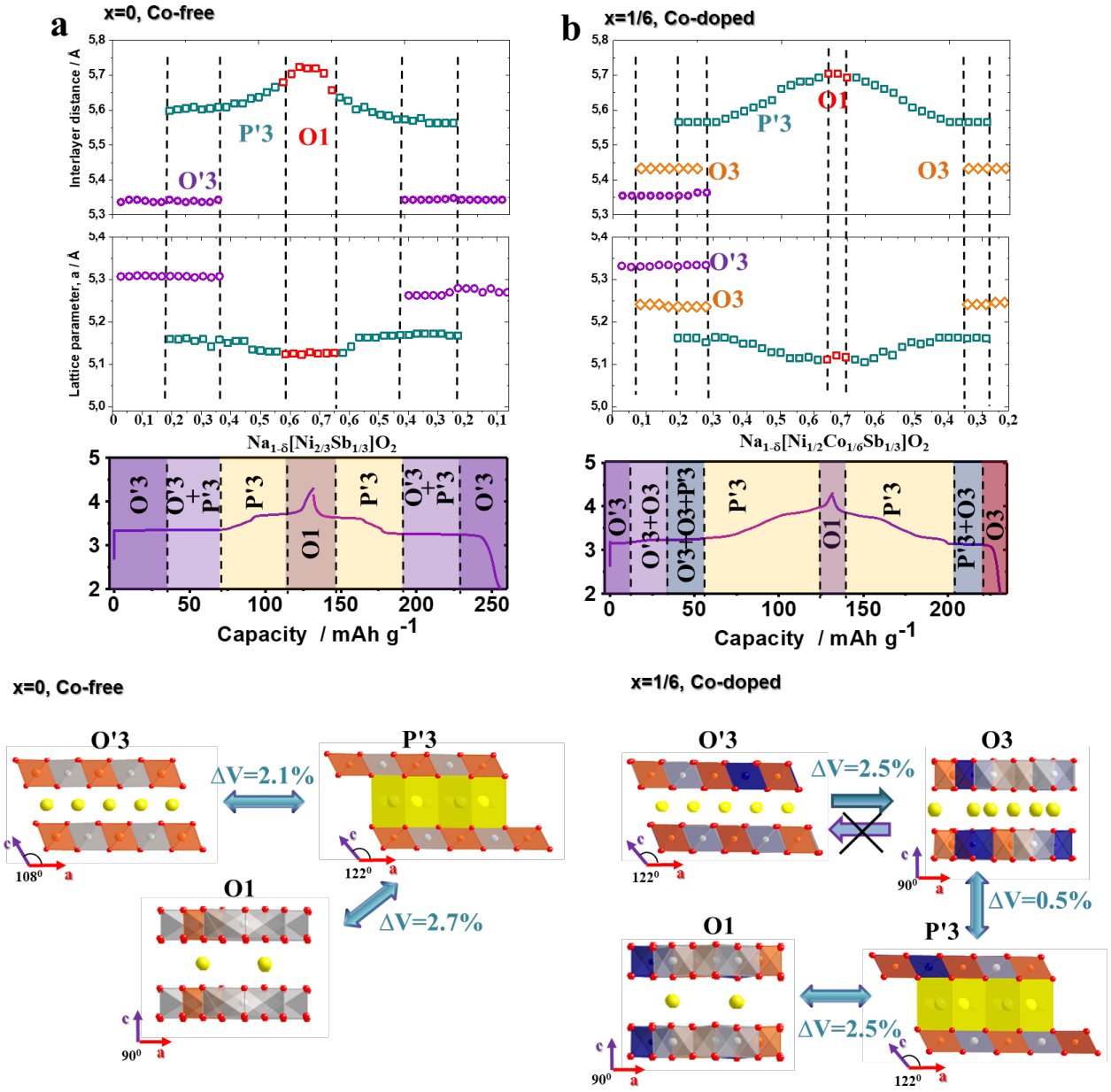

Figure 4. Calculated interslab distances and *a*-axis parameters obtained from *o*-XRD data as a function of Na^+ concentration (top), charge/discharge profiles (middle), and corresponding schematic phase transition mechanism (bottom) for (a) $Na[Ni_{2/3}Sb_{1/3}]O_2$; (b) $Na[Ni_{1/2}Co_{1/6}Sb_{1/3}]O_2$.

As it is evident from the *o*-XRD data, the major differences between $Na[Ni_{2/3}Sb_{1/3}]O_2$ and $Na[Ni_{1/2}Co_{1/6}Sb_{1/3}]O_2$ are in the appearance of hexagonal O3 phase on charge and discharge, extension of the solid solution region of P'3 phase, and shortened activity of O1 phase for the $Na[Ni_{1/2}Co_{1/6}Sb_{1/3}]O_2$. Indeed, the phase transformation from monoclinic P'3 to hexagonal O1 phase was proceeded more smoothly for the $Na[Ni_{1/2}Co_{1/6}Sb_{1/3}]O_2$, accompanied by solid-solution behavior with a linear shift of the $(130)_{P'3}$ and $(131)_{P'3}$ XRD reflections toward higher angles and intermediate phases before reaching the final O1 phase on charge (**Figure S2**). This leads to smaller variation of the lattice parameters and volume change for the $Na[Ni_{1/2}Co_{1/6}Sb_{1/3}]O_2$, compared to those values for $Na[Ni_{2/3}Sb_{1/3}]O_2$. Specifically, the volume difference from O1-$Na_{0.34}[Ni_{1/2}Co_{1/6}Sb_{1/3}]O_2$ to O3-$Na_{0.84}[Ni_{1/2}Co_{1/6}Sb_{1/3}]O_2$ is about 3.2 %, whereas that the value from O1-$Na_{0.34}[Ni_{2/3}Sb_{1/3}]O_2$ to O'3-$Na_{0.92}[Ni_{2/3}Sb_{1/3}]O_2$ increases to 4.8 % in the unit volume during discharge **(Figure 4a and 4b).**

We also employed DFT calculation to model and study the effect of Co on mechanism during charge and discharge. To find the atomic structure of O1-$Na_{0.33}[Ni_{2/3}Sb_{1/3}]O_2$, we explored all possible arrangements for 4 Na^+ in 12 Na sites, namely $\frac{12!}{4!8!} = 495$ structures in an O1-$Na_4[Ni_8Sb_4]O_{24}$ supercell using Coulomb energy calculations. The arrangement of cations was considered to be the same as found at each O-TM-O layer of the corresponding O3 phase. For charge balancing of the O1-$Na_{0.33}[Ni_{2/3}Sb_{1/3}]O_2$, we used charge states of 1+ for Na, 3+ for Ni, 5+ for Sb, and 2- for O. By carrying out density functional theory (DFT) calculation on most favourable structure from Coulomb energy analysis, we found the lowest-energy structure. To model O1-$Na_{0.33}[Ni_{1/2}Co_{1/6}Sb_{1/3}]O_2$, we also considered the arrangement of cations to be the same as found at each O-TM-O layer of the corresponding O1 phase. Similar to the case of non-doped O1-$Na_{0.33}[Ni_{2/3}Sb_{1/3}]O_2$, we calculated electrostatic energies for 495 structures considering charge states of 1+ for 4Na, 3+ for 6Ni, 3+ for 2Co, 5+ for 4Sb, and 2-

for 24O. To find the position of Co cations, we considered an O3-$Na_{36}[Ni_{18}Co_6Sb_{12}]O_{72}$ supercell and carried out DFT calculation on 2 possible configurations: i) 2Co → 2Ni at each O-TM-O layer and ii) 6Co → 6Ni at every third O-TM-O layer. It was found that the first configuration is more favorable. Afterwards, we determined the arrangement of Na ions in O3-$Na_{30}[Ni_{18}Co_6Sb_{12}]O_{72}$ by creating $\frac{36!}{30!6!} = 1947792.$ Finally, we performed DFT-SCAN calculation on the structure with the lowest total Coulomb energy value. The most favorable structures are presented in **Figure 5**.

To find the most favorable arrangement of Na, Ni, and Sb in O'3-$Na_{0.83}[Ni_{2/3}Sb_{1/3}]O_2$, we considered a O'3-$Na_{10}[Ni_8Sb_4]O_{24}$ supercell and modeled all possible configurations with i) 10 Na^+ in 12 Na sites and ii) 6 Ni^{2+}, 2Ni^{3+}, and 4Sb^{5+} in 12 transition metal sites. The charge state of O was considered to be 2-. We created a total number of $\frac{12!}{10!2!} \cdot \frac{12!}{8!4!} \cdot \frac{8!}{6!2!} = 914760$ structures. Afterwards, we performed DFT-SCAN calculation on the determined structure with the lowest electrostatic energy. To model O3-$Na_{0.83}[Ni_{1/2}Co_{1/6}Sb_{1/3}]O_2$, we first considered an O3-$Na_9[Ni_6Sb_3]O_{18}$ supercell and determined the most favorable arrangement of Ni and Sb in TM sites. All possible configurations with 6 Ni^{2+} and 3 Sb^{5+} in 9 Ni/Sb sites. The charge states of Na and O were considered to be 1+, and 2-, respectively. We created a total number of $\frac{9!}{6!3!} = 84$ structures. Afterwards, we performed DFT calculations on the lowest electrostatic energy structure.

Our DFT-SCAN calculation results indicate that for the $Na_{0.83}[Ni_{2/3}Sb_{1/3}]O_2$ system the O'3 phase, which has been observed in the *o*-XRD result, is energetically more favorable (by 50 meV per primitive unit cell of the O3 phase) than the O3 one. However, the O3 phase is energetically more favorable (by 15 meV per primitive unit cell of the O3 phase) compared to the O'3 one for the case of $Na_{0.83}[Ni_{1/2}Co_{1/6}Sb_{1/3}]O_2$, which also agrees with the XRD data (**Figure 4b**). The calculated average magnetic moment for Co in O'3 is $\bar{\mu} = 2.65$. This could

show a charge state of 2+ in a high spin state, but μ for half of Co cations is 3.50 which is not a reasonable value and might show instability of this system. The calculated values of *a* and *c*-axes parameters with DFT-SCAN for the O'3-$Na_{0.83}[Ni_{2/3}Sb_{1/3}]O_2$, O3-$Na_{0.83}[Ni_{1/2}Co_{1/6}Sb_{1/3}]O_2$, O1-$Na_{0.33}[Ni_{2/3}Sb_{1/3}]O_2$, and O1-$Na_{0.33}[Ni_{1/2}Co_{1/6}Sb_{1/3}]O_2$ are in fair agreement with our experimental results (**Table 1**). It is found that with Co doping lattice sizes decreases slightly. These tendencies are due to the smaller size of Co^{3+} (0.545 Å, low spin) compared to Ni^{3+} (0.56 Å, low spin) and Ni^{2+} (0.69 Å, low spin). The decreases in both *a* and *c*-axis parameters from our DFT data agree with XRD data of **Figure 4**.

Table 1. Calculated lattice parameters of the charged and discharged cathodes with and without Co substitution.

System	*a* [Å]	*c* [Å]
O'3-$Na_{0.83}[Ni_{2/3}Sb_{1/3}]O_2$	5.20	5.54
O3-$Na_{0.83}[Ni_{1/2}Co_{1/6}Sb_{1/3}]O_2$	3.00	15.80
O1-$Na_{0.33}[Ni_{2/3}Sb_{1/3}]O_2$	5.09	5.58
O1-$Na_{0.33}[Ni_{1/2}Co_{1/6}Sb_{1/3}]O_2$	5.07	5.55

The transition metals valence changes in $Na[Ni_{2/3-x}Co_xSb_{1/3}]O_2$ (x = 0 and 1/6) are shown in **Figure 6** and **Figure S3**. The charged $Na_{0.34}[Ni_{2/3}Sb_{1/3}]O_2$ and $Na_{0.34}[Ni_{1/2}Co_{1/6}Sb_{1/3}]O_2$ electrodes resulted in shift of the Ni K-edge spectra toward the higher-photon-energy close to the $Li[Ni_{0.8}Co_{0.1}Mn_{0.1}]O_2$, Ni^{3+} reference, indicating that divalent Ni is oxidized to trivalent on charge and on discharge *vice versa* in **Figure 6a and 6b**. In addition, Co^{2+} was oxidized to Co^{3+} after charging to 4.3 V for the $Na_{0.34}[Ni_{1/2}Co_{1/6}Sb_{1/3}]O_2$, as the Co K edge XANES spectra shifted to higher-proton-energy. Note that the oxidized Co^{3+} was unchanged and still remained as Co^{3+} even after discharge to 2 V, $Na_{0.84}[Ni_{1/2}Co_{1/6}Sb_{1/3}]O_2$ (**Figure 5c**), suggesting the irreversibility in the oxidation state of Co within the voltage range of 2 – 4.3 V. Specifically,

the structure was not able to recover to the original O'3 phase but appeared to be hexagonal O3 phase at the end of discharge. It is interpreted that, after the oxidation Co^{2+} to Co^{3+}, the $Co^{3+/2+}$ redox pair did not occur during cycling for the $Na[Ni_{1/2}Co_{1/6}Sb_{1/3}]O_2$ electrode. Sb also did not change the binding energy as pentavalent during charge and discharge (**Figure S3**).

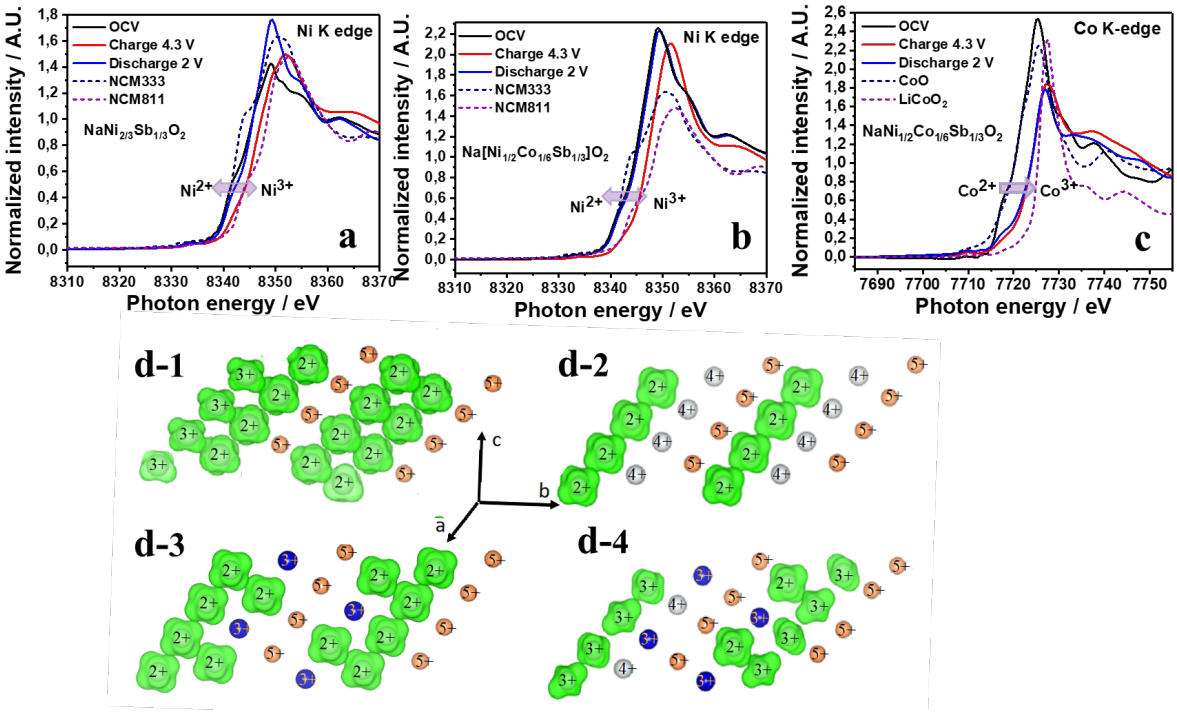

Figure 6. XANES spectra measured at OCV, charge (4.3 V) and discharge (2 V) for (a) Ni K-edge $Na[Ni_{2/3}Sb_{1/3}]O_2$; (b) Ni K-edge $[NaNi_{1/2}Sb_{1/6}Sb_{1/3}]O_2$; (c) Co K-edge $Na[Ni_{1/2}Sb_{1/6}Sb_{1/3}]O_2$; Calculated spin density plots for (d-1) O3-$Na_{0.83}[Ni_{2/3}Sb_{1/3}]O_2$; (d-2) O1-$Na_{0.33}[Ni_{2/3}Sb_{1/3}]O_2$; (d-3) O3-$Na_{0.83}[Ni_{1/2}Co_{1/6}Sb_{1/3}]O_2$, (d-4) O1-$Na_{0.33}[Ni_{1/2}Co_{1/6}Sb_{1/3}]O_2$; an isosurface of 0.06 *e* was applies. For simplicity only one O-TM-O layer is presented. Up-spin electrons are in green. Ni, Co, and Sb are in grey, blue, and orange, respectively.

We also used DFT-SCAN calculation to compute magnetic moments (the average values $\bar{\mu}$ listed in **Table 2**) and spin densities (**Figure 5 d-1-d-4**) which help us to verify the oxidation states of Ni, Co, and Sb, obtained by XANES and XPS in the structures and band magnetism. Calculated value of $\bar{\mu} \approx 0$ for Co cations in O3-$Na_{0.83}[Ni_{1/2}Co_{1/6}Sb_{1/3}]O_2$ and O1-$Na_{0.33}[Ni_{1/2}Co_{1/6}Sb_{1/3}]O_2$ show that they possess charge states of 3+, and they are in low spin

states. However, calculated magnetizations of 66.67% Co and 33.33% Co for the fully-sodiated (discharged) O3-Na$[Ni_{1/2}Co_{1/6}Sb_{1/3}]O_2$ are 2 and 4, showing intermediate and high spin states, respectively. Sb cations are most likely have charge states of 5+ because i) their computed $\bar{\mu}$ is zero (see **Table 2** and **Figures 5 d-1-d-4**) and ii) the charge neutralization is achieved only with Sb^{5+}. For the bare in the discharged state, namely O'3-$Na_{0.83}[Ni_{2/3}Sb_{1/3}]O_2$, the average charge state of 75 % of Ni is 2+ ($\bar{\mu} = 1.63\mu_B$), while that of 25 % of them is 3+ ($\bar{\mu} = 0.94\mu_B$) resulting in an average charge state of 2.25+ for Ni cations. This coincides with the expected average oxidation state of $Ni^{2.2+}$, for the discharged $Na_{0.83}[Ni_{2/3}Sb_{1/3}]O_2$. All the oxidized Ni cations are reduced back to 2+ ($\bar{\mu} = 1.64\mu_B$) after Co doping, which is in agreement with our experimental value of Ni^{2+} for the discharged O3-$Na_{0.83}[Ni_{1/2}Co_{1/6}Sb_{1/3}]O_2$. In the charged Co-free system, namely O1-$Na_{0.33}[Ni_{2/3}Sb_{1/3}]O_2$, the charge state of half Ni cations is 4+ ($\bar{\mu} = 0.01\mu_B$) while that of the rest is 2+ ($\bar{\mu} = 1.63\mu_B$); that is, the average oxidation state of Ni is 3+ that agrees with the Ni-K edge XANES data shown in **Figure 6a**. For the charged Co-doped case, O1-$Na_{0.33}[Ni_{1/2}Co_{1/6}Sb_{1/3}]O_2$, our calculations show that 66.66 % of Ni are oxidized to 3+ ($\bar{\mu} = 0.90\mu_B$), 16.67 % to 4+ ($\bar{\mu} = 0.14\mu_B$), while 16.67 % of Ni preserves their charge states to be 2+ ($\bar{\mu} = 1.58\mu_B$). In this case, the average oxidation state of Ni is 3+ that coincides fairly with the Ni-K edge XANES data of Ni^{3+} presented in **Figure 6b**.

Table 2. Calculated average magnetic moments of ions in magneton Bohr (μ_B) for the charged and discharged cathodes with and without Co substitution.

System	Na_v	Ni_w	Co_x	Sb_y	O_z
O´3-$Na_{0.83}Ni_{2/3}Sb_{1/3}O_2$	0.00	$Ni_{3/6}$→1.63 $Ni_{1/6}$→0.94		-0.00	0.06
O3-$Na_{0.83}Ni_{1/2}Co_{1/6}Sb_{1/3}O_2$	0.00	$Ni_{1/2}$→1.64	-0.01	-0.00	0.07
O1-$Na_{0.33}Ni_{2/3}Sb_{1/3}O_2$	0.00	$Ni_{1/3}$→1.63 $Ni_{1/3}$→0.01		-0.00	0.05
O1-$Na_{0.33}Ni_{1/2}Co_{1/6}Sb_{1/3}O_2$	0.00	$Ni_{1/12}$→1.58 $Ni_{4/12}$→0.90 $Ni_{1/12}$→0.14	-0.02	0.00	0.02

As mentioned in **Figure 2**, the first discharge capacities of $Na[Ni_{2/3}Sb_{1/3}]O_2$ and $Na[Ni_{1/2}Co_{1/6}Sb_{1/3}]O_2$ were 116 mAh g^{-1} and 99 mAh g^{-1}, respectively. Since the Co was active *via* the oxidation of Co^{2+} to Co^{3+} while inactive to be reduced from Co^{3+} to Co^{2+} in the operation range, the obtained capacity is smaller for the $Na[Ni_{1/2}Co_{1/6}Sb_{1/3}]O_2$. On the other hand, the electro-conducting character of Co^{3+} provides significant electro-conducting capability as the Co^{3+} t_{eg} level overlaps with the oxygen 2*p* orbital. Our calculated total density of states indicate a small shifting of the Fermi level into the top region of the valence band after Co doping of O3-$Na_{0.83}[Ni_{2/3}Sb_{1/3}]O_2$ (**Figure 7a and 7b**). This is probably due to the reduction of Ni cations that had charge states of 3+, which is induced after doping the system with Co^{3+}. Impact of Co-doping is, however, significant after charging since no band gap is observed for O1-$Na_{0.33}[Ni_{1/2}Co_{1/6}Sb_{1/3}]O_2$ showing a much higher electronic conductivity for the charged case after Co doping (**Figure 7c and 7d**). Accordingly, the electrochemical-driven Co^{3+} affects its conductivity throughout the oxide matrix, such that the $Na[Ni_{1/2}Co_{1/6}Sb_{1/3}]O_2$ electrode was able to demonstrates not only excellent capacity retention but also high rate capability up to 50 C-rates in **Figure 2**. The calculated diffusion coefficients reveal the readiness of Na^+ diffusion in the $Na[Ni_{1/2}Co_{1/6}Sb_{1/3}]O_2$ structure; namely, the diffusion was improved by a factor of ~10^{-10} – ~10^{-12} S cm^{-1} for the $Na[Ni_{2/3}Sb_{1/3}]O_2$ and ~10^{-9} – ~10^{-12} S

cm^{-1} $Na[Ni_{1/2}Co_{1/6}Sb_{1/3}]O_2$ (**Figure S4a and S4b**). From the diffusivity, it is likely that the oxidation of Co^{2+} to Co^{3+} occurs when Na^+ extraction was initiated in the range of $y = 0 – 0.08$ in $Na_{1-y}[Ni_{1/2}Co_{1/6}Sb_{1/3}]O_2$, prior to the formation of O3 phase, because the diffusion became faster after the emergence of the O3 phase that shows higher diffusivity during further cycle. This result reveals the electrochemical-driven Co^{3+} formation is beneficial to enhance Na^+ kinetics.

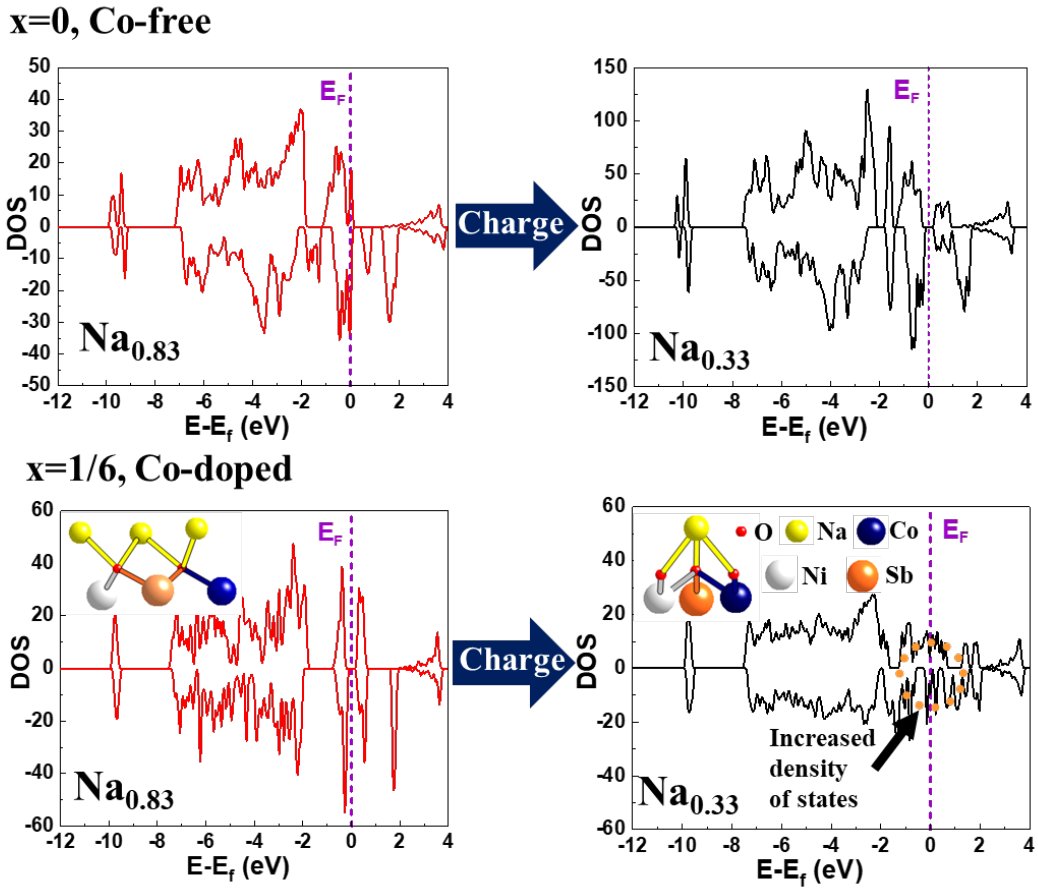

Figure 7. Total density of states for (a) O3-$Na_{0.83}[Ni_{2/3}Sb_{1/3}]O_2$ (b) O1-$Na_{0.33}[Ni_{2/3}Sb_{1/3}]O_2$ (c) O3-$Na_{0.83}[Ni_{1/2}Co_{1/6}Sb_{1/3}]O_2$ (d) O1-$Na_{0.33}[Ni_{1/2}Co_{1/6}Sb_{1/3}]O_2$.

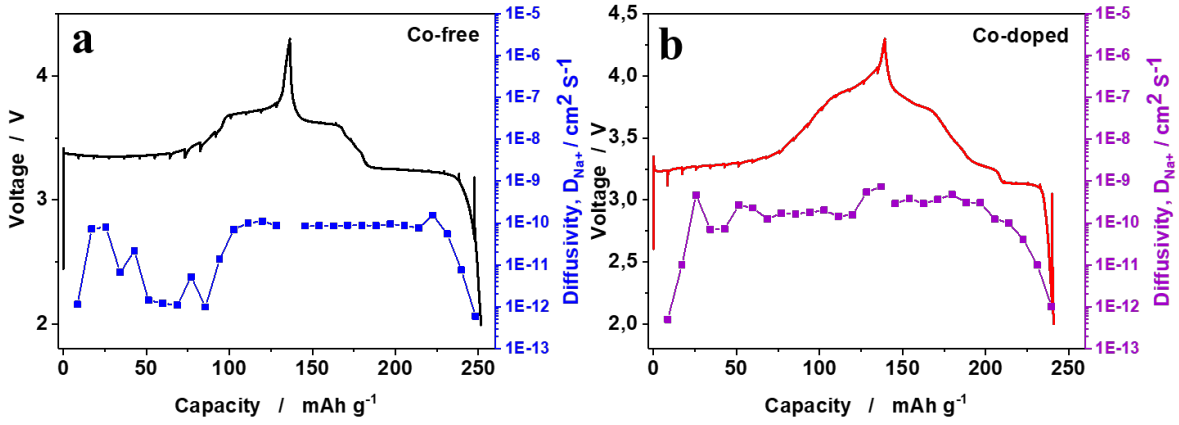

Figure S4. GITT curves and calculated Na^+ diffusion coefficients for (a) $Na[Ni_{2/3}Sb_{1/3}]O_2$; (b) $Na[Ni_{1/2}Sb_{1/6}Sb_{1/3}]O_2$.

Furthermore, in consideration of Gibbs free energy for formation at 298 K $Ni^{2+}O$, $Co^{2+}O$, and $Co_3^{2.67+}O_4$ have -211.7 kJ mol^{-1}, -214.0 kJ mol^{-1}, and -774 kJ mol^{-1}. Although it is not possible to directly compare due to lack of the thermodynamic data for Co_2O_3, it can be deduced that the formation of Co^{3+} in the oxide matrix can improve the bond strength between metal and oxygen in the $Na[Ni_{1/2}Co_{1/6}Sb_{1/3}]O_2$ compound. This simultaneously suppresses movement of the interslabs at highly charged states such for P'3 and O1 phase (**Figure 4b**). As a result, the less change in the structure could delay the deterioration of the active materials during cycling so as to result in better capacity retention, as confirmed in the XRD patterns of the $Na[Ni_{2/3}Sb_{1/3}]O_2$ and $Na[Ni_{1/2}Co_{1/6}Sb_{1/3}]O_2$ electrodes after 100 and 1,000 cycles (**Figure S4**). In addition, the presence of the strong bonding induced by Co^{3+}-O may increase repulsion between sodium ions in the structure, thereby resulting in the increased operation voltage from 3.6 V to 3.9 V. This phenomenon is usually observed when stronger bonds present in compounds, as Goodenough et al.[40,41] observed in metal oxides and metal sulfides and Ceder et al.[42] and we observed in Al-doped transition metal oxides.[43,44]

As a result, the related reaction can be summarized as a 2/3 sodium extraction through the

reversible O'3 ↔ P'3 ↔ O1 phase transformations for the $Na[Ni_{2/3}Sb_{1/3}]O_2$. However, for the $Na[Ni_{1/2}Co_{1/6}Sb_{1/3}]O_2$, a 1/2 sodium extraction through the O3 ↔ P'3 ↔ O1 phase transformation occurred. The irreversible O'3 → O3 transformation in the $Na[Ni_{1/2}Co_{1/6}Sb_{1/3}]O_2$ is attributed to the irreversible Co^{3+}/Co^{2+} reaction; however, the electrochemical-driven Co^{3+} contributes to remarkable improvement in structural stability and electrode performance for long term and even at high rates.

3. Conclusions

A solid solution of $Na[Ni_{2/3}Sb_{1/3}]O_2 - Na[Co_{2/3}Sb_{1/3}]O_2$ is investigated as cathode materials for SIBs. The similarity in the ionic radii between Ni^{2+} (0.69 Å) and Co^{2+} (0.74 Å) enables formation of the solid solution in full range, although the main redox moiety is limited to the $Ni^{3+/2+}$ redox pair. Due to difficulty of the redox of $Co^{3+/2+}$, the oxidized Co^{3+} remains throughout the oxide matrix in $Na[Ni_{2/3-x}Co_xSb_{1/3}]O_2$, such that the resulting electric conductivity contributes to facile Na^+ diffusion up to a 50 C-rate. Furthermore, the electrochemical-driven Co^{3+} endorses structural stabilization to suppress the phase transition and expansion of the interslab distance to lead excellent cyclability for long term. This finding suggests the rational design of electrochemical-driven Co^{3+}-substituted materials can be useful in development other high performance electrode materials for rechargeable batteries.

4. Experimental

4.1. Synthesis

$Na[Ni_{2/3-x}Co_xSb_{1/3}]O_2$ ($x = 0 - 2/3$) were synthesized *via* a conventional solid-state process using Na_2CO_3 (Sigma Aldrich), NiO (Sigma Aldrich), Co_3O_4 (Sigma Aldrich), and Sb_2O_3 (Sigma Aldrich). A stoichiometric amount of each starting material was thoroughly mixed with

high energy ball-mill at 350 rpm in ethanol for 3 h. Subsequently, ethanol was evaporated at 120 °C, and the resultant was dried in an oven at 120 °C for overnight. Finally, the powders were pelletized and calcined at 1000 °C for 12 h in O_2.

4.2. Material characterization

X-ray diffraction was performed to determine the crystal structure of $Na[Ni_{2/3-x}Co_xSb_{1/3}]O_2$ (x = 0 – 2/3) using a PANalytical X'Pert diffractometer with a Cu Kα source, radiating from 10 to 80° (2θ) at a step size of 0.03°. The obtained XRD data were refined using FULLPROF program.[45] Morphologies of as-synthesized powders were observed using scanning electron microscopy (SEM; SU-8010, Hitachi) and high-resolution TEM (H-800, Hitachi) coupled with energy-dispersive X-ray (EDX) spectrometry. Structural studies during cycling were performed using *operando* XRD (X'Pert, PANalytical diffractometer, 14°–50° (2θ)), *ex situ* X-ray photoelectron spectroscopy (PHI 5600, Perkin-Elmer), and *ex situ* X-ray absorption near-edge structure spectroscopy (XANES). XANES analyses for the Ni K-edge and Co K-edge region were performed in a transmission mode at beamline 8C at Pohang Accelerator Laboratory (PAL), South Korea.

4.3. Electrochemical characterization

The $Na[Ni_{2/3-x}Co_xSb_{1/3}]O_2$ (x = 0 – 2/3) powders were mixed with Super P and polyvinylidene fluoride (PVDF) binder in the ratio 8 : 1 : 1 (wt. %) in *N*-methyl-2-pyrrolidone (NMP). The homogeneous mixtures were applied on aluminum (Al) foil using a doctor blade and were then dried at 120 °C for overnight in vacuum oven. The $Na[Ni_{2/3-x}Co_xSb_{1/3}]O_2$ electrodes were paired with Na metal in R2032 coin-type cells, separated by Whatman GF/C glass fiber in 0.5 mol dm^{-3} $NaPF_6$ in propylene carbonate (PC) and fluoroethylene carbonate (FEC) (98:2 in volume). Assembly of coin cells was carried out in an Ar-filled glove box

with H_2O and O_2 contents < 0.1 ppm. Galvanostatic charge and discharge measurements were conducted in the voltage range of 2–4.3 V at 25 °C applying different currents 0.05 –50C (1C = 200 mA g^{-1}). Galvanostatic intermittent titration technique (GITT) measurements were performed with 30-min charge and discharge and relaxation periods of 1h at a current density of 0.05C.

4.4. *Computation*

Spin-polarized density functional theory (DFT) calculations were performed using the projector augmented wave (PAW)[46] potential method implemented in the Vienna *Ab Initio* Simulation Package (VASP) code.[47] The Strongly Constrained and Appropriately Normed (SCAN) functional was used. To perform Coulomb and DFT calculation on charged and discharged systems, we used [2√3×3]-type ($Na_{10}Ni_8Sb_4O_{24}$), [2√3×2√3] R30-type ($Na_{30}Ni_{18}Co_6Sb_{12}O_{72}$), [2√3×2√3] R30-type ($Na_4Ni_8Sb_4O_{24}$), and [2√3×2√3] R30-type ($Na_4Ni_6Co_2Sb_4O_{24}$) supercells to model O´3-$Na_{0.83}Ni_{2/3}Sb_{1/3}O_2$, O3-$Na_{0.83}Ni_{1/2}Co_{1/6}Sb_{1/3}O_2$, O1-$Na_{0.33}Ni_{2/3}Sb_{1/3}O_2$, and O1-$Na_{0.33}Ni_{1/2}Co_{1/6}Sb_{1/3}O_2$, respectively. To find the arrangement of Ni, Co and Sb in the O3 structure we had to use a [√3×√3] R30-type ($Na_9Ni_6Co_2Sb_4O_{18}$) supercell to reduce the huge number of combinations. Gamma-centered *k*-point meshes of 2×2×4, 2×2×2, and 2×2×4 were applied for O'3, O3, and O1 structures, respectively. An energy cutoff of 600 eV as well as electronic and force convergence criteria of 10^{-4} eV and 10^{-3} eV/Å, respectively, were considered for DFT calculations. Total Coulomb energy calculations were carried out using the so-called *supercell* code.[48] Atomic structures were visualized with VESTA program.[49]

Acknowledgements

This work was supported by the Basic Science Research Program through the National

Research Foundation of Korea (NRF), funded by the Ministry of Education, Science, and Technology of Korea (NRF 2015M3D1A1069713, NRF 2017R1E1A2A01079404, NRF 2017M2A2A6A01070834 and NRF 2017K1A3A1A30084795).

Appendix A. Supplementary data

Supplementary data to this article can be found online at

References

[1] K. Kubota, S. Kumakura, Y. Yoda, K. Kuroki, S. Komaba, *Advanced Energy Materials* 2018, *8*, 1.

[2] J. Y. Hwang, S. T. Myung, Y. K. Sun, *Chemical Society Reviews* 2017, *46*, 3529.

[3] N. Ortiz-Vitoriano, N. E. Drewett, E. Gonzalo, T. Rojo, *Energy and Environmental Science* 2017, *10*, 1051.

[4] T. Jin, H. Li, K. Zhu, P. F. Wang, P. Liu, L. Jiao, *Chemical Society Reviews* 2020, *49*, 2342.

[5] N. Voronina, J. H. Jo, J. U. Choi, A. Konarov, J. Kim, S. T. Myung, *Journal of Power Sources* 2020, *455*, 227976.

[6] G. Yan, S. Mariyappan, G. Rousse, Q. Jacquet, M. Deschamps, R. David, B. Mirvaux, J. W. Freeland, J. M. Tarascon, *Nature Communications* 2019, *10*.

[7] N. Voronina, J. H. Jo, J. U. Choi, C. H. Jo, J. Kim, S. T. Myung, *Journal of Materials Chemistry A* 2019, *7*, 5748.

[8] L. Wang, Y. Lu, J. Liu, M. Xu, J. Cheng, D. Zhang, J. B. Goodenough, *Angewandte Chemie - International Edition* 2013, *52*, 1964.

[9] Q. Liu, Z. Hu, M. Chen, C. Zou, H. Jin, S. Wang, S. L. Chou, Y. Liu, S. X. Dou, *Advanced Functional Materials* 2020, *30*, 1.

[10] A. Manthiram, J. B. Goodenough, *Journal of Solid State Chemistry* 1987, *71*, 349.

[11] C. Masquelier, L. Croguennec, *Chemical Reviews* 2013, *113*, 6552.

[12] J. Kim, G. Yoon, M. H. Lee, H. Kim, S. Lee, K. Kang, *Chemistry of Materials* 2017, *29*, 7826.

[13] H. Park, J. K. Yoo, W. Ko, Y. Lee, I. Park, S. T. Myung, J. Kim, *Journal of Power Sources* 2019, *434*, 226750.

[14] J. Qian, C. Wu, Y. Cao, Z. Ma, Y. Huang, X. Ai, H. Yang, *Advanced Energy Materials* 2018, *8*, 1.

[15] P. F. Wang, Y. You, Y. X. Yin, Y. G. Guo, *Advanced Energy Materials* 2018, *8*, 1.

[16] S. Wang, C. Sun, N. Wang, Q. Zhang, *Journal of Materials Chemistry A* 2019, *7*, 10138.

[17] J. U. Choi, C. S. Yoon, Q. Zhang, P. Kaghazchi, Y. H. Jung, K. S. Lee, D. C. Ahn, Y. K. Sun, S. T. Myung, *Journal of Materials Chemistry A* 2019, *7*, 202.

[18] A. Konarov, J. U. Choi, Z. Bakenov, S. T. Myung, *Journal of Materials Chemistry A* 2018, *6*, 8558.

[19] A. Konarov, H. J. Kim, N. Voronina, Z. Bakenov, S. T. Myung, *ACS Applied Materials and Interfaces* 2019, *11*, 28928.

[20] A. Konarov, H. J. Kim, J. H. Jo, N. Voronina, Y. Lee, Z. Bakenov, J. Kim, S. T. Myung, *Advanced Energy Materials* 2020, *10*, 1.

[21] J. H. Jo, J. U. Choi, Y. J. Park, J. Zhu, H. Yashiro, S. T. Myung, *ACS Applied Materials and Interfaces* 2019, *11*, 5957.

[22] C. H. Jo, J. U. Choi, H. Yashiro, S. T. Myung, *Journal of Materials Chemistry A* 2019, *7*, 3903.

[23] M. H. Han, E. Gonzalo, M. Casas-Cabanas, T. Rojo, *Journal of Power Sources* 2014, *258*, 266.

[24] L. Wang, J. Wang, X. Zhang, Y. Ren, P. Zuo, G. Yin, J. Wang, *Nano Energy* 2017, *34*, 215.

[25] P. Vassilaras, D. H. Kwon, S. T. Dacek, T. Shi, D. H. Seo, G. Ceder, J. C. Kim, *Journal of Materials Chemistry A* 2017, *5*, 4596.

[26] P. Zhou, X. Liu, J. Weng, L. Wang, X. Wu, Z. Miao, J. Zhao, J. Zhou, S. Zhuo, *Journal of Materials Chemistry A* 2019, *7*, 657.

[27] L. Zheng, R. Fielden, J. C. Bennett, M. N. Obrovac, *Journal of Power Sources* 2019, *433*, 0.

[28] J. Y. Hwang, C. S. Yoon, I. Belharouak, Y. K. Sun, *Journal of Materials Chemistry A* 2016, *4*, 17952.

[29] M. Sathiya, Q. Jacquet, M. L. Doublet, O. M. Karakulina, J. Hadermann, J. M. Tarascon, *Advanced Energy Materials* 2018, *8*, 1.

[30] S. Komaba, N. Yabuuchi, T. Nakayama, A. Ogata, T. Ishikawa, I. Nakai, *Inorganic Chemistry* 2012, *51*, 6211.

[31] M. Keller, D. Buchholz, S. Passerini, *Advanced Energy Materials* 2016, *6*, 1.

[32] S. Mariyappan, T. Marchandier, F. Rabuel, A. Iadecola, G. Rousse, A. V. Morozov, A. M. Abakumov, J. M. Tarascon, *Chemistry of Materials* 2020, *32*, 1657.

[33] Y. You, S. O. Kim, A. Manthiram, *Advanced Energy Materials* 2017, *7*, 1.

[34] F. Aguesse, J. M. Lopez del Amo, L. Otaegui, E. Goikolea, T. Rojo, G. Singh, *Journal of Power Sources* 2016, *336*, 186.

[35] D. S. Bhange, G. Ali, D. H. Kim, D. A. Anang, T. J. Shin, M. G. Kim, Y. M. Kang, K. Y. Chung, K. W. Nam, *Journal of Materials Chemistry A* 2017, *5*, 1300.

[36] P. F. Wang, Y. J. Guo, H. Duan, T. T. Zuo, E. Hu, K. Attenkofer, H. Li, X. S. Zhao, Y. X. Yin, X. Yu, Y. G. Guo, *ACS Energy Letters* 2017, *2*, 2715.

[37] P. F. Wang, H. Xin, T. T. Zuo, Q. Li, X. Yang, Y. X. Yin, X. Gao, X. Yu, Y. G. Guo,

Angewandte Chemie - International Edition 2018, *57*, 8178.

[38] D. Yuan, X. Liang, L. Wu, Y. Cao, X. Ai, J. Feng, H. Yang, *Advanced Materials* 2014, *26*, 6301.

[39] V. V. Politaev, V. B. Nalbandyan, A. A. Petrenko, I. L. Shukaev, V. A. Volotchaev, B. S. Medvedev, *Journal of Solid State Chemistry* 2010, *183*, 684.

[40] J. B. Goodenough, *Solid State Ionics* 1994, *69*, 184.

[41] A. Manthiram, J. B. Goodenough, *Journal of Power Sources* 1989, *26*, 403.

[42] G. Ceder, Y. M. Chiang, D. R. Sadoway, M. K. Aydinol, Y. I. Jang, B. Huang, *Nature* 1998, *392*, 694.

[43] S.-T. Myung, S. Komaba, N. Kumagai, *Journal of The Electrochemical Society* 2001, *148*, A482.

[44] J. H. Jo, Y. K. Sun, S. T. Myung, *Journal of Materials Chemistry A* 2017, *5*, 8367.

[45] J. Rodríguez-Carvajal, *Physica B: Physics of Condensed Matter* 1993, *192*, 55.

[46] P. E. Blöchl, *Physical Review B* 1994, *50*, 17953.

[47] G. Kresse, J. Furthmüller, *Computational Materials Science* 1996, *6*, 15.

[48] K. Okhotnikov, T. Charpentier, S. Cadars, *Journal of Cheminformatics* 2016, *8*, 1.

[49] K. Momma, F. Izumi, *Journal of Applied Crystallography* 2011, *44*, 1272.